Check for updates

Change in Structure of Amorphous Sb–Te Phase-Change Materials as a Function of Stoichiometry

Shehzad Ahmed, Xudong Wang,* Heming Li, Yuxing Zhou, Yuhan Chen, Liang Sun, Wei Zhang,* and Riccardo Mazzarello*

Chalcogenide phase-change materials (PCMs) are a leading candidate for non-volatile memory and neuro-inspired computing applications. Antimony telluride alloys can be made into fast and robust PCMs by proper doping. Depending on the compositional ratio, the amorphous state of these alloys shows either nucleation- or growth-driven crystallization dynamics at elevated temperatures. In this work, thorough ab initio simulations are carried out to study the structural properties and bonding nature of six Sb–Te alloys with varied composition from 2:3 to 4:1. Despite all of the compounds showing similar local structural motifs consisting of defective octahedral configurations, a gradual change in medium range order and cavity concentration is observed as the Sb content increases. This trend is responsible for the reduction in the nucleation rate, thus leading to growth-driven crystallization. In addition, the degree of charge transfer decreases as the composition approaches the Sb end, reducing the driving force for long-term mass transport and phase separation upon extensive cycling in devices.

1. Introduction

The concept of phase-change memory using chalcogenide glasses dates back to the 1960s, as pioneered by Ovshinsky.[1] Starting from late 1980s, Ge–Sb–Te alloys along the GeTe–Sb_2Te_3 pseudo-binary line (Group I), such as $Ge_2Sb_2Te_5$, $Ge_1Sb_2Te_4$ and $Ge_8Sb_2Te_{11}$,[2–5] doped Sb_{2+x}-Te alloys (Group

II), such as Ag-, In-doped $Sb_{2+x}Te$ (AIST), and alloyed Sb (Group III),[6–10] such as $Ge_{15}Sb_{85}$, were identified as suitable PCMs. These alloys were initially used for the rewritable optical data storage industry.[11] More recently, the $Ge_1Sb_2Te_4$ (GST) alloy has been used as the core material for electronic non-volatile memories,[12–19] e.g., 3D Xpoint. Moreover, PCMs can be used for neuro-inspired computing and in-memory computing,[20–27] and could also enable various nonvolatile photonic applications, including memory and computing devices, switches, and displays.[28–36]

PCMs utilize the significant contrast in electrical resistivity or optical reflectivity between their crystalline and amorphous phase to encode data.[11] The switching between the two logic states is achieved by rapid and reversible phase transitions, namely, SET (crystallization) and RESET (melt-quenched amorphization). In addition to binary storage, multiple resistivity or reflectivity states can be obtained within a PCM cell via partial amorphization (iterative RESET) and crystallization (accumulative SET), enabling multilevel storage[37,38] and neuro-inspired computing applications.[39,40]

S. Ahmed, X. Wang, H. Li, Y. Zhou, Y. Chen, Prof. W. Zhang
Center for Alloy Innovation and Design (CAID)
State Key Laboratory for Mechanical Behavior of Materials
Xi'an Jiaotong University
Xi'an 710049, China
E-mail: xudong.wang@stu.xjtu.edu.cn; wzhang0@mail.xjtu.edu.cn

S. Ahmed, X. Wang, H. Li, Y. Zhou, Y. Chen
Materials Studio for Neuro-Inspired Computing
School of Materials Science and Engineering
Xi'an Jiaotong University
Xi'an 710049, China

Y. Chen, Prof. R. Mazzarello
Department of Physics
Sapienza University of Rome
Rome 00185, Italy
E-mail: riccardo.mazzarello@uniroma1.it

Dr. L. Sun
Key Laboratory of Materials Processing Engineering
College of Materials Science and Engineering
Xi'an Shiyou University
Xi'an 710065, China

Prof. R. Mazzarello
Institute for Theoretical Solid-State Physics
JARA-FIT and JARA-HPC
RWTH Aachen University
Aachen 52056, Germany
E-mail: mazzarello@physik.rwth-aachen.de

ADVANCED SCIENCE NEWS
www.advancedsciencenews.com

pss
physica status solidi rrl
www.pss-rapid.com

Group I PCMs show nucleation-driven crystallization at elevated temperatures that are relevant for practical use. For instance, GST and $Ge_2Sb_2Te_5$ can crystallize in tens of nanoseconds in ≈100 nm memory cells via formation of multiple nuclei by electrical pulsing or laser irradiation.[12] Upon rapid crystallization, Group I PCMs form a rocksalt-like structure,[41–46] where Te atoms sit on the sites of one sublattice, while Ge, Sb and atomic vacancies occupy the other sublattice in a random fashion. The high nucleation rate in Group I PCMs stems from the abundant presence of crystalline precursors, i.e., ABAB squares (A = Ge or Sb, B = Te), in the amorphous phase.[47–59] By further enhancing the stability of such crystalline precursors, a Sc doped Sb_2Te_3 alloy with ultrahigh nucleation rate has been designed, which breaks down the switching time to subnanosecond regime.[60–67]

Moving toward the Sb corner in the Ge–Sb–Te ternary diagram, group II and III PCMs show much lower nucleation tendency, and crystallization proceeds mostly from the crystalline-amorphous boundaries with high growth rates.[68–78] To explain the fast growth in these PCMs, in particular, AIST, a bond-interchange model was proposed, in which small displacements of Sb atoms accompanied by interchanges of short and long bonds occur.[69] *Ab initio* simulations indicate that the rapid crystal growth in the supercooled liquid regime originates from the combination of high mass diffusivity, effective atomic attaching process due to the large driving force and thin crystalline-amorphous interfaces.[78,79]

Thus, there is a change in crystallization mechanism in Sb–Te alloys upon tuning the stoichiometry from Sb_2Te_3 to Sb-rich compounds. To elucidate this trend, we carry out comprehensive density functional theory (DFT) calculations and DFT-based ab initio molecular dynamics (AIMD) simulations of Sb–Te alloys with composition varying from 2:3 to 4:1. We investigate the structural and bonding properties of the crystalline and amorphous state of these compounds. We also determine the evolution of the crystalline precursors in the amorphous phase as a function of Sb concentration, providing an atomistic picture of how the crystallization mode changes from nucleation- to growth-type.

2. Results and Discussion

We perform AIMD calculations using the second-generation Car–Parrinello method,[80] as implemented in the CP2K package.[81,82] The Perdew–Burke–Ernzerhof (PBE) functional[83] and the Goedecker pseudopotentials[84] are used. The time step is set as 2 fs. The amorphous models and corresponding crystalline structures are relaxed using the VASP code,[85] prior to the electronic-structure and chemical-bonding calculations. For VASP calculations, the projector augmented-wave (PAW) pseudopotentials[86] and the same PBE functional are used. The energy cutoff for plane waves is set as 500 eV. The crystalline phase calculations are done using k point meshes ranging from $13 \times 13 \times 3$ to $13 \times 13 \times 1$ (less k points are used for the Sb–Te crystals with more extended c lattice), whereas only the Γ point is used to sample the Brillouin zone of the amorphous models in cubic supercells. Chemical bonding analyses are made using the crystal orbital overlap population (COOP) method,[87] as implemented in the LOBSTER code.[88–90] All the data presented below are obtained using the PBE functional. The calculations of the crystalline models are cross-checked by including van der Waals corrections,[91] as shown in **Figure 1** and **2** of the Supporting Information.

The crystalline (c-) structures of the six Sb–Te crystals are shown in Figure 1. The stable phase of Sb_2Te_3 is rhombohedral, and consists of alternately stacked Sb and Te atoms forming quintuple-layer (QL) blocks along the c axis. The QLs are separated by van der Waals (vdW)-like gaps. The unit cell of Sb_2Te_3 contains 3 QLs and 3 such gaps.[92] Besides the stable rhombohedral phase, a metastable rocksalt-like phase is known for Sb_2Te_3, in which 1/3 lattice sites in the Sb sublattice are vacant (Figure S3, Supporting Information).[93,94] The Sb_8Te_9 crystal shows a very long c lattice parameter (>10 nm) with 3 alternately stacked atomic blocks, each of which contains 3 Sb_2Te_3 QLs + 1 Sb_2 bilayer (BL).[95] Regarding c-Sb_4Te_3, two stacking sequences are known. Both phases consist of 3 alternately stacked blocks. In the first phase, the block contains 2 Sb_2Te_3 QLs + 2 Sb_2 BLs (thereby, a vdW-like gap in between the QLs), whereas, in the second phase, the block consists of 1 Sb_2Te_3 QL + 1 Sb_2 BL (no vdW-like gap is present). In experiments, c-Sb_4Te_3 shows a mixture of the two stacking sequences.[96] Indeed, our simulations show that the two phases are very close in energy: the former structure (Figure 1) is only ≈4 meV atom^{-1} lower in energy than the latter (Figure S4, Supporting Information). The primitive cell of the Sb_2Te crystal consists of 1 Sb_2Te_3 QL and 2 Sb_2 BLs, and the number of Sb_2 BLs increases further in the primitive cells of c-Sb_3Te and c-Sb_4Te.[97] Note that the Sb slabs in c-Sb_3Te contain an even number of layers. Odd numbers of Sb layers would raise the energy by ≈61 meV atom^{-1}.

The PBE-relaxed structures yield very similar a lattice parameters ≈4.35 Å for the six Sb–Te crystals, while the c parameter varies from ≈17.79 to ≈104.76 Å depending on the size of the atomic blocks and the periodic conditions. In all six crystals, Sb atoms show a distorted octahedral configuration in both Sb_2Te_3 QLs and Sb_2 BLs. The ratio of Sb–Sb homopolar bonds (Sb–Te heteropolar bonds) increases (decreases) as the concentration of Sb increases. All Sb atoms exhibit Peierls-like distortions. For instance, Sb–Te bond lengths of ≈3.00/≈3.20 Å are found in Sb_2Te_3 QLs, Sb–Sb contacts of length ≈2.96/≈3.42 Å are found in Sb_2 BLs, and Sb–Sb and Sb–Te contacts of length ≈2.96 and ≈3.55 Å, respectively, are observed at the QL/BL interfaces in c-Sb_2Te. Te atoms are either in a distorted octahedral configuration or in a defective octahedral configuration with only 3 neighbors due to the presence of vdW-like gaps. In c-Sb_2Te_3, The Te–Te contact across the vdW-like gap between two QLs has length equal to ≈3.93 Å. To summarize, all atoms form a distorted octahedral bonding configuration, and ABAB squares with nearly 90° bond angles are consistently found in these rhombohedral Sb–Te crystals and in rocksalt Sb_2Te_3. Inclusion of vdW corrections leads to non-negligible changes in the c parameter, due to the reduction in the size of the vdW-like gaps between weakly coupled Te layers (Figure S1, Supporting Information).

As shown in Figure 2a, the calculated density of states (DOS) indicate that all the six crystals are narrow bandgap semiconductors. The COOP analysis[87] separates the covalent interactions into bonding (right side) and antibonding (left side)
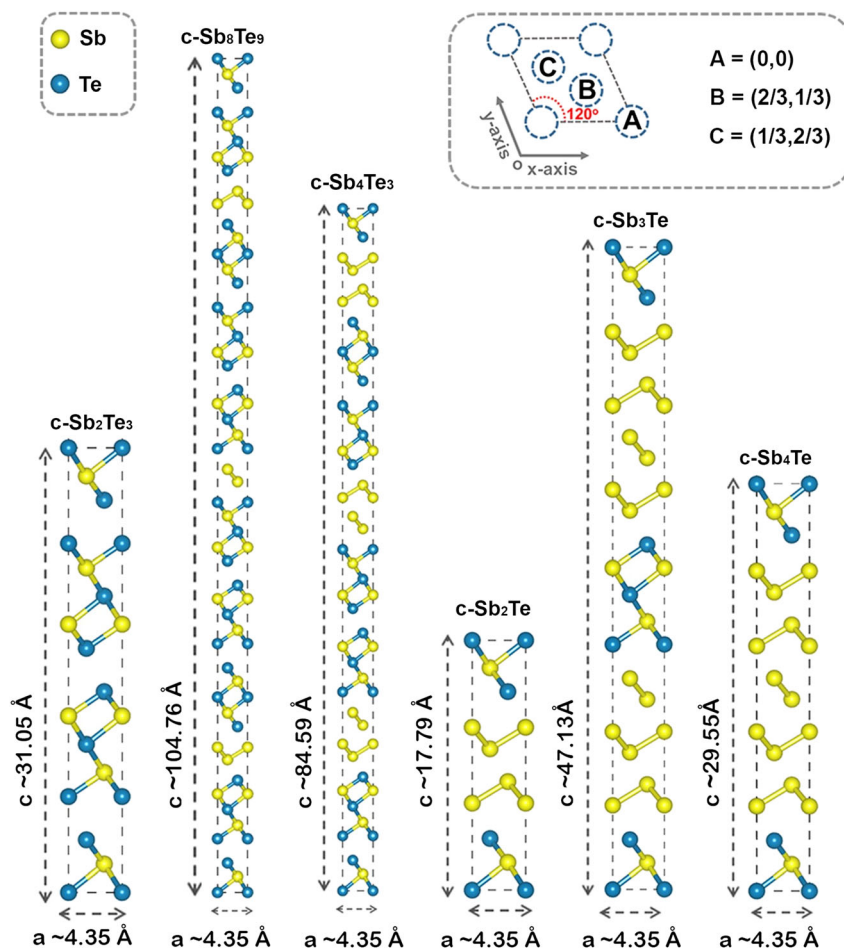
Figure 1. Crystal structures of six Sb–Te alloys in the hexagonal cell setup, including Sb_2Te_3, Sb_8Te_9, Sb_4Te_3, Sb_2Te, Sb_3Te and Sb_4Te. The rhombohedral Sb_2Te_3 contains 3 Sb_2Te_3 QLs separated by vdW-like gaps. In crystalline Sb_8Te_9, Sb_4Te_3, Sb_2Te, Sb_3Te and Sb_4Te, A7-type Sb slabs are stacked along the c axis and sandwiched by Sb_2Te_3 QL blocks. Three typical atomic positions in the a-b plane of the hexagonal cell are shown in the top view of the unit cell (top right panel).
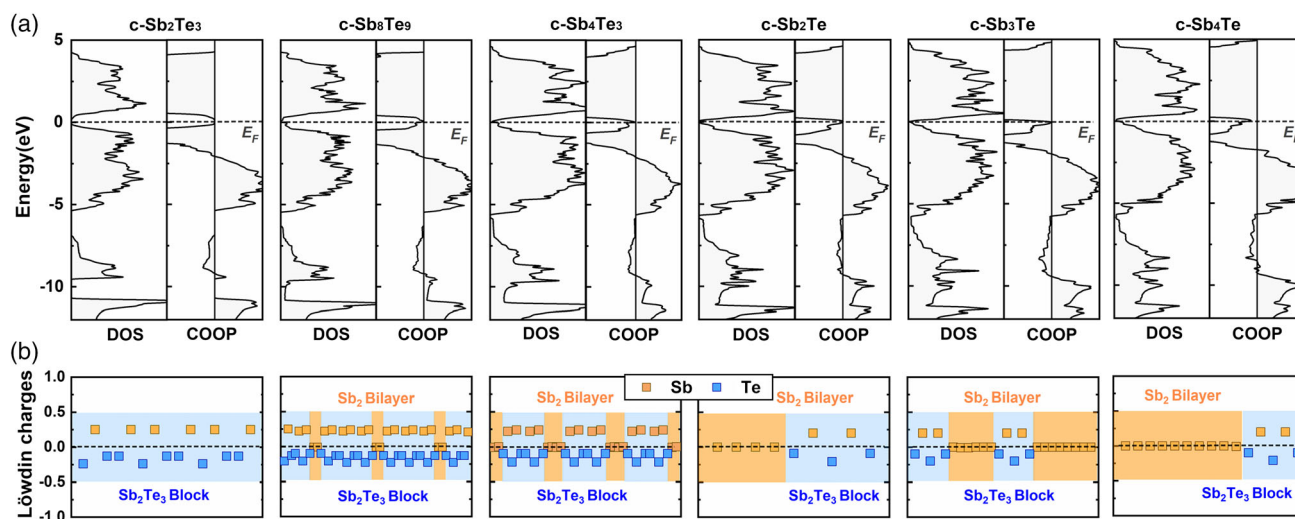

Figure 2. Electronic structure, chemical bonding and charge analysis for Sb_2Te_3, Sb_8Te_9, Sb_4Te_3, Sb_2Te, Sb_3Te and Sb_4Te in the rhombohedral form. a) DOS and COOP. b) Löwdin charges for each individual atom in the unit cell.

contributions, as shown in Figure 2a. The marginal antibonding interactions at the Fermi level E_F suggest that all these structures are chemically stable. Löwdin charges are calculated to assess the charge transfer and the electrostatic interactions in these alloys (Figure 2b). In Sb_2Te_3 QLs, moderate charge transfers are found, resulting in slightly positively (negatively) charged Sb (Te) atoms, while, in Sb-rich compounds, the Sb atoms in the BLs remain almost neutral. The distribution of the Löwdin charges in the six Sb–Te crystals are rather similar, except that the fraction of neutral Sb_2 increases gradually from c-Sb_2Te_3 to c-Sb_4Te. Calculations with vdW corrections yield very similar DOS, COOP curves and Löwdin charges (Figure S2, Supporting Information).

The amorphous models of the six Sb–Te alloys are generated via the melt-quench protocol, following our previous work.[61,98] Three independent amorphous models are generated for each Sb–Te composition to obtain better statistical sampling. Each amorphous model contains 180 atoms in a cubic supercell with varied Sb and Te concentrations. The calculated edge length values are 18.92, 18.82, 18.68, 18.63, 18.59, and 18.56 Å for amorphous Sb_2Te_3, Sb_8Te_9, Sb_4Te_3, Sb_2Te, Sb_3Te, and Sb_4Te, respectively. These values were obtained by relaxing the internal pressure below ≈1 kbar. Snapshots for the six amorphous alloys are shown in **Figure 3**a, and the total and partial radial distribution functions (RDFs) are shown in Figure 3b. The Sb–Sb and Sb–Te RDFs show nearly identical peak positions at ≈2.92 Å for the first peak and at ≈4.25 Å for the second peak. The Te–Te RDFs of the six models differ from each other, in that short Te-Te contacts gradually vanish as the Sb concentration increases.

The calculated DOS and COOP for the six amorphous alloys are shown in **Figure 4**a. Similarly to their crystalline counterparts, these amorphous alloys are narrow-gap semiconductors. The COOP curves indicate reasonable chemical stability for all the models. Previous work has shown that non-negligible charge transfer is observed in the amorphous state,[99,100] which causes long-term mass transport of Sb and Te atoms toward opposite directions upon extensive electrical pulsing in devices, resulting in the formation of voids at the bottom electrode and segregation

of Sb atoms close to the top electrode.[101] As shown in Figure 4b, the Löwdin charge distributions show a gradual change in the average charge of Sb from ≈0.189 in a-Sb_2Te_3 to ≈0.033 in a-Sb_4Te, while that of Te fluctuates around –0.13 for the six models. The reduction in average charge for the Sb atoms and the decrease in Te concentration in Sb-rich alloys are expected to reduce the long-term mass transport. In the extreme case of pure Sb,[102–105] the absence of charge transfer should lead to much improved cycling performance.

By integrating the projected COOP for a specific pair of atoms A and B over all occupied orbitals along the energy axis up to E_F, the bond population $B_{AB} = \int_{-\infty}^{E_F} COOP_{AB}(E)dE$ is obtained, which characterizes the strength of the covalent interaction between the two atoms. As shown in **Figure 5**, the overall bonding profiles look similar for all the six amorphous alloys. The B_{AB} distributions for Sb–Te and Sb–Sb contacts strongly overlap with each other. The shorter the interatomic distance, the higher the bond population. Following our previous work,[106–108] we multiply the B_{AB} by the RDF and obtain the "bond-weighted distribution function" $BWDF = \sum_{B>A}[\delta(r - |r_{AB}|) \times B_{AB}]$ for the six amorphous alloys. The crossover from positive to negative values in the BWDFs determines a threshold for covalent interactions. For all the six amorphous alloys, the threshold values for both Sb–Te and Sb–Sb contacts are found at ≈3.20 Å. These crossover values are used as cutoffs for the following analyses. The vast majority of Te–Te contacts shows antibonding character.

Figure 6 shows the angle distribution functions (ADFs) and the fraction of homopolar and heteropolar bonds in the amorphous alloys. Clearly, all the Sb and Te atoms show bond angles close to ≈90° or ≈180°. The bond order analysis using the parameter $q = 1 - \frac{3}{8}\sum_{B>A}\left(\frac{1}{3} + \cos\theta_{ABC}\right)^2$ between three atoms A, B and C, indicates that Sb and Te atoms are primarily found in defective octahedral configurations in all six amorphous alloys, resembling the local structures in their crystalline counterparts. As the Sb concentration increases, more Sb neighbors are found in the Sb-centered octahedral motifs, as indicated by the insets shown in Figure 6a. The fraction of Sb–Sb bonds increases from ≈8% in a-Sb_2Te_3 to ≈71% in a-Sb_4Te, and the fraction of Sb–Te and Te–Te bonds decreases accordingly (Figure 6b).
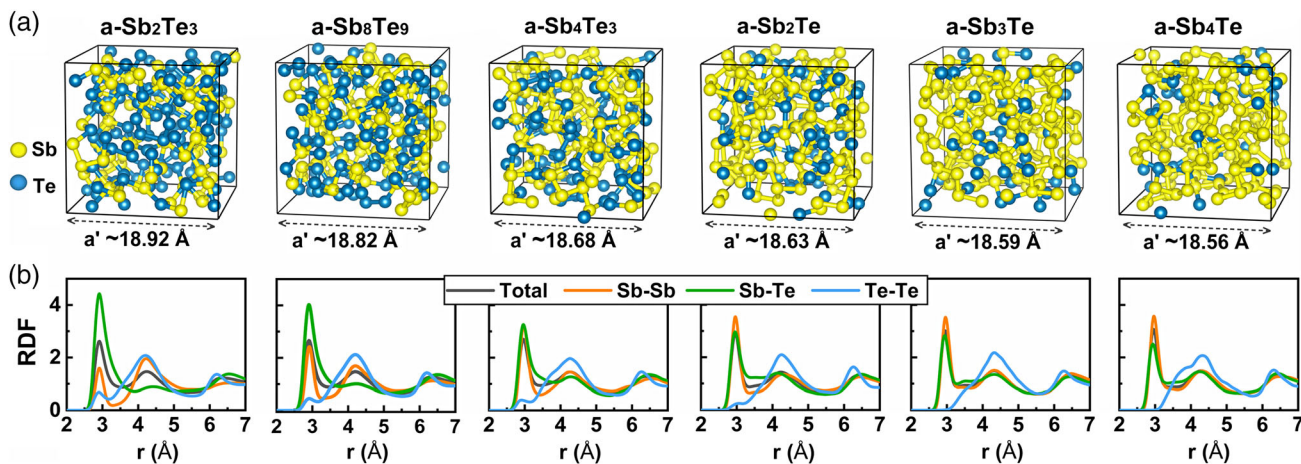

Figure 3. a) Snapshots of amorphous Sb_2Te_3, Sb_8Te_9, Sb_4Te_3, Sb_2Te, Sb_3Te and Sb_4Te from melt-quench AIMD simulations. b) Total and partial RDFs of the six amorphous alloys based on AIMD trajectories at 300 K.
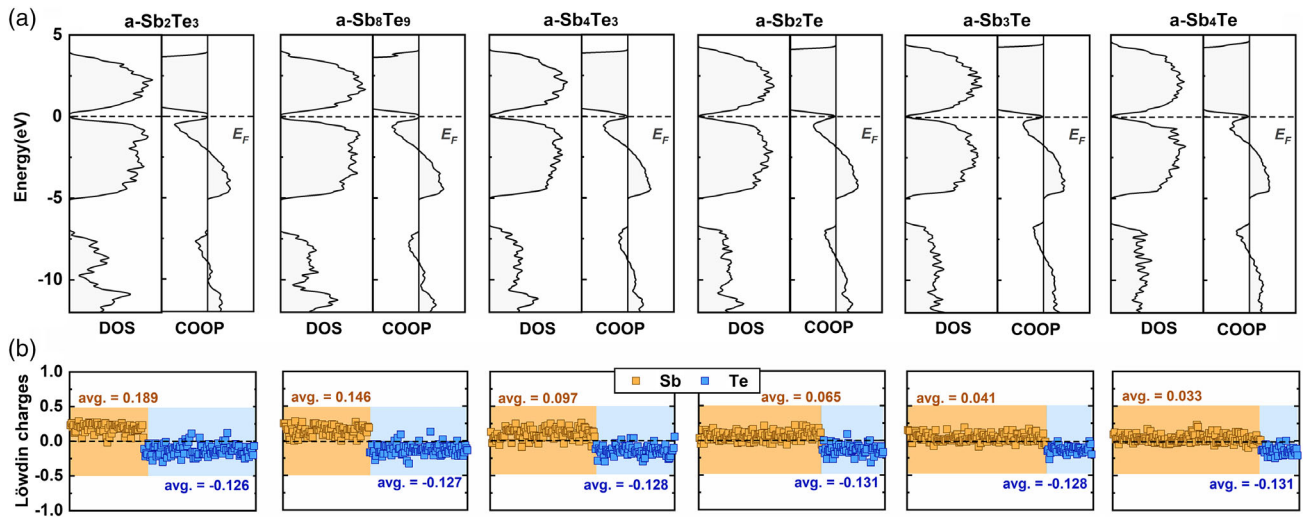
Figure 4. Electronic structure, chemical bonding and charge analysis of amorphous Sb_2Te_3, Sb_8Te_9, Sb_4Te_3, Sb_2Te, Sb_3Te and Sb_4Te. a) DOS and COOP. b) Löwdin charges for each individual atom in the amorphous models.
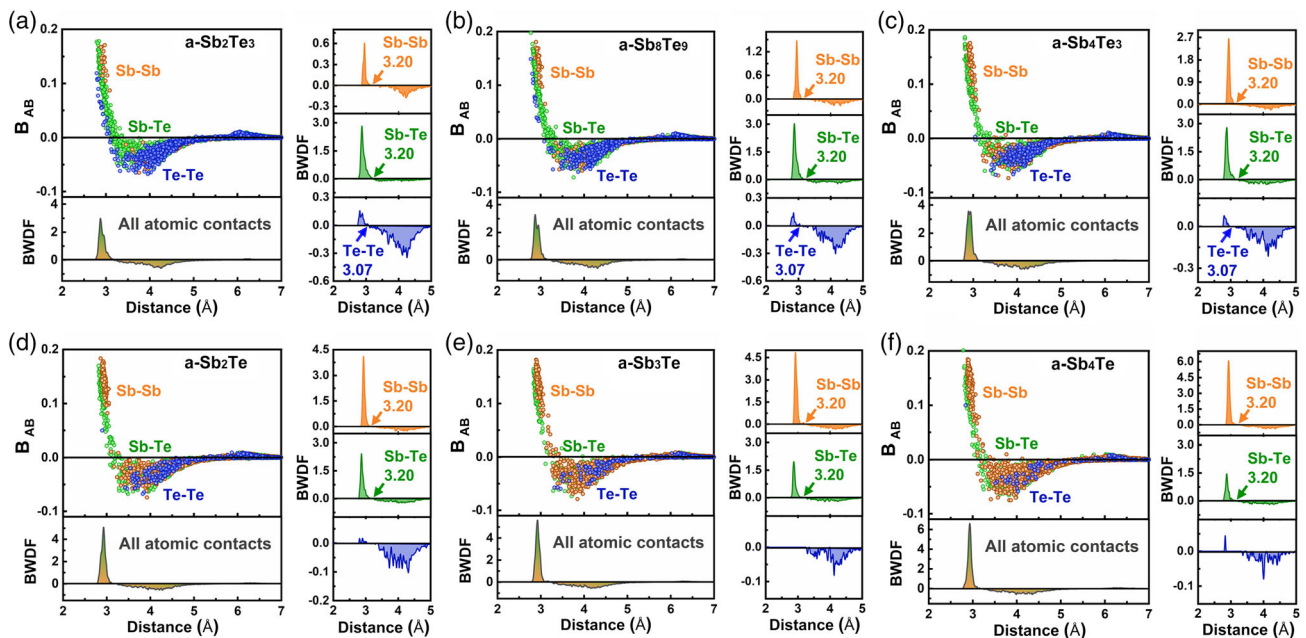
Figure 5. a–f) The bond population B_{AB}, total and partial BWDF of amorphous Sb_2Te_3 (a), Sb_8Te_9 (b), Sb_4Te_3 (c), Sb_2Te (d), Sb_3Te (e) and Sb_4Te (f). The B_{AB} and BWDF of the six amorphous alloys are calculated for all the atomic contacts up to 7 Å.

The primitive ring statistics is typically used to assess the medium-range order in amorphous PCMs. As shown in **Figure 7**a, fourfold rings dominate in amorphous Sb_2Te_3, Sb_8Te_9 and Sb_4Te_3, while fivefold rings become richer in amorphous Sb_2Te, Sb_3Te and Sb_4Te. A detailed analysis of the fraction of ABAB squares (A = Sb, B = Te) with respect to the total number of fourfold rings is shown in **Table 1**. The abundance of ABAB squares promotes rapid incubation of crystalline nuclei in a-Sb_2Te_3 at elevated temperatures, allowing short SET time within 6 ns in ≈150 nm memory cells.[60] As the Sb concentration increases, the fraction of ABAB squares sharply decreases from ≈81% in a-Sb_2Te_3 to ≈34% in a-Sb_4Te_3, and nearly vanishes in a-Sb_4Te with only ≈2% value, despite that fourfold rings are still abundant in the amorphous network (Table 1). This reduction is due to the increase in Sb–Sb homopolar bonds in Sb-rich Sb–Te alloys. Moreover, fivefold rings showing non-90 bond angles (Figure 7b) become abundant, like in AIST.[69] Such ring fragments are absent in the corresponding crystalline phase. The more pronounced structural dissimilarity between the two phases in Sb-rich compounds may increase the
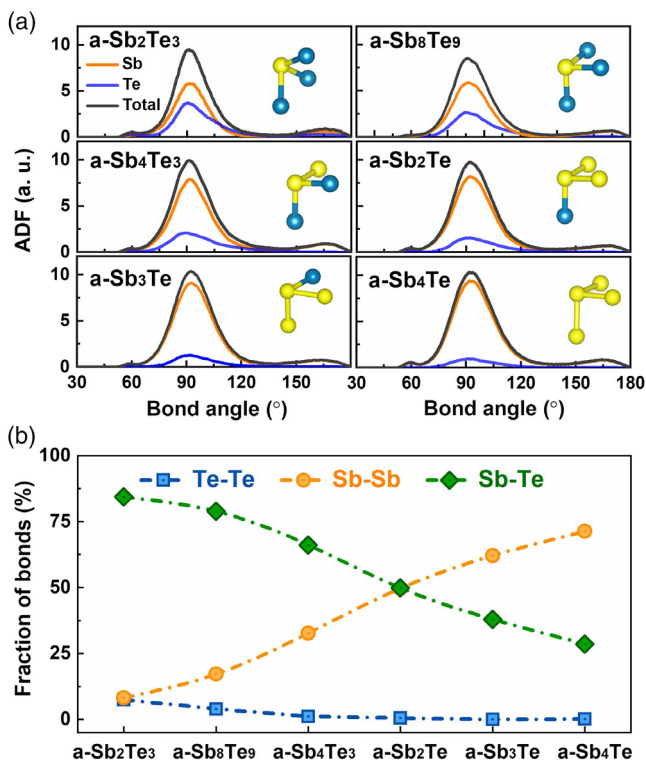
ADVANCED
SCIENCE NEWS

www.advancedsciencenews.com

pss rrl
physica status solidi

www.pss-rapid.com

Figure 6. a) The angle distribution function (ADF). The typical local atomic motifs around Sb and Te atoms are shown as insets. b) Fraction of homopolar (Sb–Te) and heteropolar (Sb–Sb and Te–Te) bonds.

Table 1. The statistics of different types of fourfold rings in the six amorphous Sb–Te alloys.

Fourfold rings		Fraction [%]					
		a-Sb$_2$Te$_3$	a-Sb$_8$Te$_9$	a-Sb$_4$Te$_3$	a-Sb$_2$Te	a-Sb$_3$Te	a-Sb$_4$Te
ABAB	Sb–Te–Sb–Te	80.8	63.7	34.1	21.0	11.0	1.8
Non-ABAB	Sb–Te–Te–Te	2.1	0.4	0.0	0.0	0.0	0.0
	Sb–Sb–Te–Te	4.0	2.7	1.4	0.5	0.1	0.2
	Sb–Sb–Sb–Te	13.1	31.2	55.8	50.3	43.9	42.5
	Sb–Sb–Sb–Sb	0.0	2.0	8.7	28.2	45.0	55.5
	Te–Te–Te–Te	0.0	0.0	0.0	0.0	0.0	0.0

cells, in which the small amorphous mark is surrounded by a crystalline matrix, crystallization occurs by rapid interfacial growth from the crystalline-amorphous boundaries.

The crystallization scenario could be more complex in a-Sb$_8$Te$_9$, which could fall in a transition regime from nucleation-type to growth-type. The very much extended structure of c-Sb$_8$Te$_9$ shown in Figure 1 was obtained experimentally by long-term thermal annealing at 800 °C.[95] This structure displays a very similar atomic arrangement of the QL blocks as rhombohedral Sb$_2$Te$_3$. The latter is also obtained at very high annealing temperatures over long annealing time. Starting from the amorphous phase of Sb$_2$Te$_3$, the thermal energy at elevated temperatures firstly drives a rapid transition into the metastable rocksalt phase, then induces a second transition toward the layered rhombohedral phase via vacancy ordering,[94] similarly to the behavior of GST.[109–111] The high concentration of atomic vacancies in rocksalt Sb$_2$Te$_3$ and GST ensures that the average number of valence p electrons per site is equal to 3.[94,112] This configuration

interfacial energy and, thus, reduce the probability of formation of sizable nuclei on short timescales. As a result, in phase-change
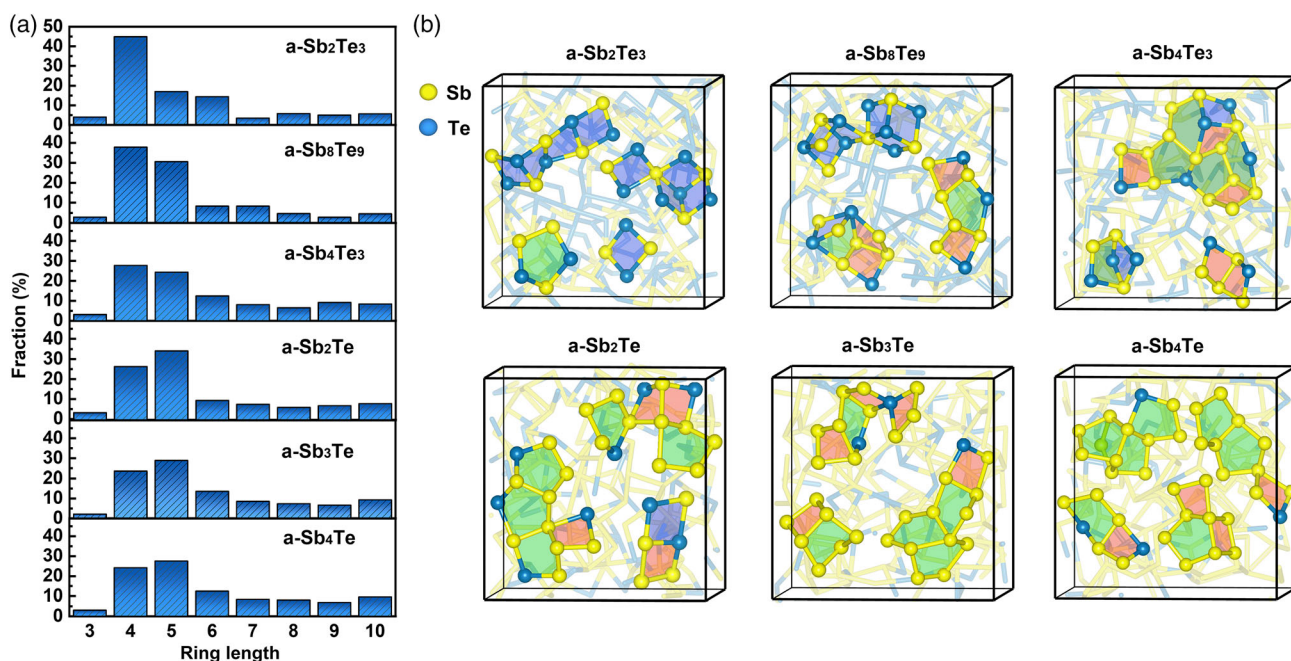

Figure 7. a) The fraction of primitive rings for the six amorphous Sb–Te alloys. b) Different types of rings in the amorphous networks are highlighted, including ABAB squares (blue), non-ABAB rings (red), and 5-membered rings (green).
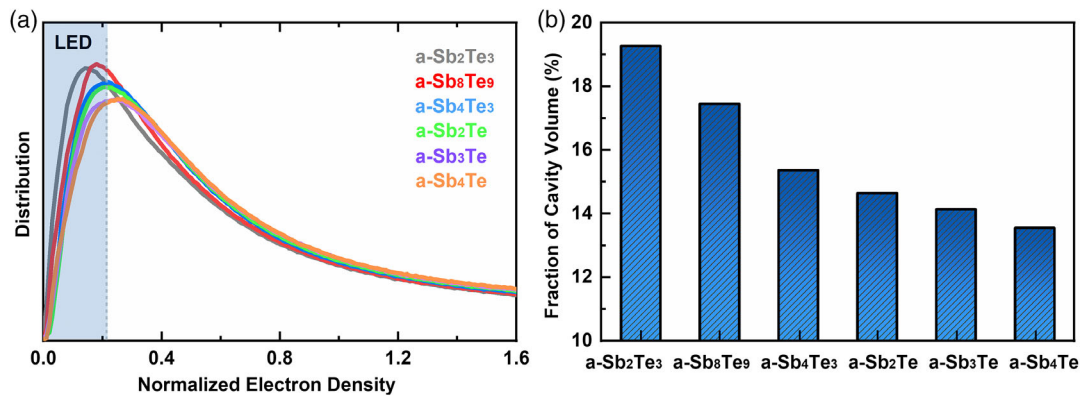
Figure 8. Cavity analysis for the six amorphous Sb–Te alloys. a) Distribution of normalized electron density. A cavity region is defined as a volume with normalized electron density smaller than the threshold value of 0.24 (shaded area). b) The fraction of cavity volume with respect to the total volume of the simulation box.

enables metavalent bonding,[113–117] which is a generic bonding mechanism in crystalline PCMs. If a rocksalt Sb_8Te_9 structure is built, the excess p electrons brought by the additional Sb atoms push up the E_F into the antibonding region, inducing some chemical instability (Figure S3, Supporting Information). Taking into account the reduced ABAB-ring fraction ($\approx 64\%$) in the amorphous state, it remains unclear whether rapid nucleation into the rocksalt phase via formation of ABAB squares and cubes could occur at the elevated temperatures relevant for practical applications. Nevertheless, a recent work on Sb–Te thin films claims the formation of rocksalt $Sb_{2+x}Te_3$ ($x \leq 1$) upon thermal annealing at 120–180 °C, whereas, when x becomes greater than 1, a direct transition from the amorphous to the rhombohedral phase occurs without the intermediate rocksalt phase.[118]

Lastly, we present an analysis of the cavity distribution in amorphous Sb–Te alloys. The high fraction of cavities in amorphous $Ge_2Sb_2Te_5$ could provide free space for rapid rearrangement of atoms, which could assist the incubation process.[48] To calculate the volume fraction of cavities in the six amorphous Sb–Te alloys, we follow the electron density method developed in Ref. [119]. Cavities are characterized by low electron density (LED). By setting a threshold value for LED, the volume of cavities is obtained. In rocksalt Sb_2Te_3, atomic vacancies occupy 1/6 of the lattice points. We tune the threshold value of the normalized electron density D^e, i.e., the absolute electron density at any given point normalized by the average electron density of the system, in a rocksalt Sb_2Te_3 model until the volume of the LED regions reaches $\approx 16.67\%$ of the whole supercell volume. The obtained D^e is 0.24, which coincides with that determined for rocksalt $Ge_2Sb_2Te_5$.[119] **Figure 8**a shows the distribution of D^e, and the integration up to the threshold value 0.24 gives the volume fraction of the LED regions (i.e., the cavities). Figure 8b shows the cavity volume fraction for the six amorphous alloys. A gradual decrease is observed from $\approx 19.1\%$ in a-Sb_2Te_3 to $\approx 14.5\%$ in a-Sb_2Te and to $\approx 13.3\%$ in a-Sb_4Te. We note that the value for a-Sb_2Te is much larger than that reported in our previous work,[120] primarily because supercell models with volume corresponding to the experimental density were used in ref. [120].

3. Conclusions

We have carried out thorough ab initio calculations to assess the structural and bonding characteristics of crystalline and amorphous Sb–Te alloys with the Sb:Te ratio ranging from 2:3 to 4:1. We show that similar distorted and/or defective octahedral motifs are found in all crystalline and amorphous Sb–Te alloys. Amorphous Sb_2Te_3 contains a very large fraction of ABAB rings, which facilitates nucleation. In contrast, medium-range structural dissimilarities between the two phases are observed in Sb_4Te_3, Sb_2Te, Sb_3Te and Sb_4Te, since the amorphous networks contain significant fractions of fivefold rings. This dissimilarity could explain the suppression of nucleation in these Sb-rich Sb–Te alloys, as a result of which the crystallization is governed by interface growth. In Sb_8Te_9, the fraction of ABAB squares is reduced and the chemical stability of the rocksalt phase is poorer as compared to Sb_2Te_3, nevertheless nucleation could still play a role in devices. Therefore, our results suggest that either a compositional threshold or a more extended nucleation-to-growth crossover should exist between the 2:3 and 1:1 ratio for Sb–Te alloys, due to the changes in the amorphous network and the increasing structural dissimilarities with respect to the crystalline phase. Furthermore, the crossover region should depend on the device geometry and size, since the smaller the switching part, the less relevant nucleation processes are. Further research efforts on this crossover region will be helpful for the design of optimal device geometries for improved SET performance.

Supporting Information

Supporting Information is available from the Wiley Online Library or from the author.

Conflict of Interest

The authors declare no conflict of interest.

Data Availability Statement

Research data are not shared.

[1] S. Ovshinsky, *Phys. Rev. Lett.* **1968**, *21*, 1450.
[2] M. Chen, K. A. Rubin, R. W. Barton, *Appl. Phys. Lett.* **1986**, *49*, 502.
[3] N. Yamada, E. Ohno, N. Akahira, K. Nishiuchi, K. Nagata, M. Takao, *Jpn. J. Appl. Phys. Part 1* **1987**, *26*, 61.
[4] N. Yamada, E. Ohno, K. Nishiuchi, N. Akahira, M. Takao, *J. Appl. Phys.* **1991**, *69*, 2849.
[5] N. Yamada, T. Matsunaga, *J. Appl. Phys.* **2000**, *88*, 7020.
[6] H. Iwasaki, M. Harigaya, O. Nonoyama, Y. Kageyama, M. Takahashi, K. Yamada, H. Deguchi, Y. Ide, *Jpn. J. Appl. Phys. Part 1* **1993**, *32*, 5241.
[7] T. Matsunaga, Y. Umetani, N. Yamada, *Phys. Rev. B* **2001**, *64*, 184116.
[8] C. N. Afonso, J. Solis, F. Catalina, C. Kalpouzos, *Appl. Phys. Lett.* **1992**, *60*, 3123.
[9] K. Sokolowski-Tinten, J. Solis, J. Bialkowski, J. Siegel, C. N. Afonso, D. V. D. Linde, *Phys. Rev. Lett.* **1998**, *81*, 3679.
[10] L. van Pieterson, M. H. R. Lankhorst, M. van Schijndel, A. E. T. Kuiper, J. H. J. Roosen, *J. Appl. Phys.* **2005**, *97*, 083520.
[11] M. Wuttig, N. Yamada, *Nat. Mater.* **2007**, *6*, 824.
[12] H.-S. P. Wong, S. Raoux, S. B. Kim, J. Liang, J. P. Reifenberg, B. Rajendran, M. Asheghi, K. E. Goodson, *Proc. IEEE* **2010**, *98*, 2201.
[13] S. Raoux, W. Welnic, D. Ielmini, *Chem. Rev.* **2010**, *110*, 240.
[14] W. Zhang, E. Ma, *Mater. Today* **2020**, *41*, 156.
[15] G. W. Burr, M. BrightSky, A. Sebastian, H. Cheng, J. Wu, S. Kim, N. Sosa, N. Papandreou, H. S. Lung, H. Pozidis, E. Eleftheriou, C. Lam, *IEEE J. EM. Sel. Top. C.* **2016**, *6*, 146.
[16] E. C. Ahn, H. S. P. Wong, E. Pop, *Nat. Rev. Mater.* **2018**, *3*, 18009.
[17] W. Zhang, M. Wuttig, *Phys. Status Solidi RRL* **2019**, *13*, 1900130.
[18] X.-B. Li, N.-K. Chen, X.-P. Wang, H.-B. Sun, *Adv. Funct. Mater.* **2018**, *28*, 1803380.
[19] K. J. Yoon, Y. Kim, C. S. Hwang, *Adv. Electron. Mater.* **2019**, *5*, 1800914.
[20] A. Sebastian, M. Le Gallo, G. W. Burr, S. Kim, M. BrightSky, E. Eleftheriou, *J. Appl. Phys.* **2018**, *124*, 111101.
[21] W. Zhang, R. Mazzarello, M. Wuttig, E. Ma, *Nat. Rev. Mater.* **2019**, *4*, 150.
[22] A. Sebastian, M. Le Gallo, R. Khaddam-Aljameh, E. Eleftheriou, *Nat. Nanotechnol.* **2020**, *15*, 529.
[23] Y. Zhang, Z. Wang, J. Zhu, Y. Yang, M. Rao, W. Song, Y. Zhuo, X. Zhang, M. Cui, L. Shen, R. Huang, J. Joshua Yang, *Appl. Phys. Rev.* **2020**, *7*, 011308.
[24] Z. Zhang, Z. Wang, T. Shi, C. Bi, F. Rao, Y. Cai, Q. Liu, H. Wu, P. Zhou, *InfoMat* **2020**, *2*, 261.
[25] J. Zhu, T. Zhang, Y. Yang, R. Huang, *Appl. Phys. Rev.* **2020**, *7*, 011312.
[26] M. Xu, X. Mai, J. Lin, W. Zhang, Y. Li, Y. He, H. Tong, X. Hou, P. Zhou, X. Miao, *Adv. Funct. Mater.* **2020**, *30*, 2003419.
[27] K. Ding, J. Wang, Y. Zhou, H. Tian, L. Lu, R. Mazzarello, C. Jia, W. Zhang, F. Rao, E. Ma, *Science* **2019**, *366*, 210.
[28] M. Wuttig, H. Bhaskaran, T. Taubner, *Nat. Photonics* **2017**, *11*, 465.
[29] P. Hosseini, C. D. Wright, H. Bhaskaran, *Nature* **2014**, *511*, 206.
[30] C. Ríos, M. Stegmaier, P. Hosseini, D. Wang, T. Scherer, C. D. Wright, H. Bhaskaran, W. H. P. Pernice, *Nat. Photonics* **2015**, *9*, 725.
[31] J. Feldmann, N. Youngblood, C. D. Wright, H. Bhaskaran, W. H. P. Pernice, *Nature* **2019**, *569*, 208.
[32] J. Feldmann, N. Youngblood, M. Karpov, H. Gehring, X. Li, M. Stappers, M. Le Gallo, X. Fu, A. Lukashchuk, A. S. Raja, J. Liu, C. D. Wright, A. Sebastian, T. J. Kippenberg, W. H. P. Pernice, H. Bhaskaran, *Nature* **2021**, *589*, 52.
[33] B. Gholipour, *Science* **2019**, *366*, 186.
[34] J. Tian, H. Luo, Y. Yang, F. Ding, Y. Qu, D. Zhao, M. Qiu, S. I. Bozhevolnyi, *Nat. Commun.* **2019**, *10*, 396.
[35] H. Zhang, L. Zhou, L. Lu, J. Xu, N. Wang, H. Hu, B. M. A. Rahman, Z. Zhou, J. Chen, *ACS Photonics* **2019**, *6*, 2205.
[36] Y. Zhang, J. B. Chou, J. Li, H. Li, Q. Du, A. Yadav, S. Zhou, M. Y. Shalaginov, Z. Fang, H. Zhong, C. Roberts, P. Robinson, B. Bohlin, C. Ríos, H. Lin, M. Kang, T. Gu, J. Warner, V. Liberman, K. Richardson, J. Hu, *Nat. Commun.* **2019**, *10*, 4279.
[37] A. Athmanathan, M. Stanisavljevic, N. Papandreou, H. Pozidis, E. Eleftheriou, *IEEE J. Emerg. Sel. Topics Circuits Syst.* **2016**, *6*, 87.
[38] X. Sun, A. Lotnyk, M. Ehrhardt, J. W. Gerlach, B. Rauschenbach, *Adv. Opt. Mater.* **2017**, *5*, 1700169.
[39] W. Zhang, R. Mazzarello, E. Ma, *MRS Bull.* **2019**, *44*, 686.
[40] D. Wright, H. Bhaskaran, W. Pernice, *MRS Bull.* **2019**, *44*, 721.
[41] N. Yamada, *MRS Bull.* **1996**, *21*, 48.
[42] B. J. Kooi, W. M. G. Groot, J. T. M. D. Hosson, *J. Appl. Phys.* **2004**, *95*, 924.
[43] B. Zhang, W. Zhang, Z.-J. Shen, Y.-J. Chen, J.-X. Li, S.-B. Zhang, Z. Zhang, M. Wuttig, R. Mazzarello, E. Ma, X.-D. Han, *Appl. Phys. Lett.* **2016**, *108*, 191902.
[44] U. Ross, A. Lotnyk, E. Thelander, B. Rauschenbach, *Appl. Phys. Lett.* **2014**, *104*, 121904.
[45] A. Lotnyk, M. Behrens, B. Rauschenbach, *Nanoscale Adv.* **2019**, *1*, 3836.
[46] M. Zhu, K. Ren, L. Liu, S. Lv, X. Miao, M. Xu, Z. Song, *Phys. Rev. Mater.* **2019**, *3*, 033603.
[47] S. Kohara, K. Kato, S. Kimura, H. Tanaka, T. Usuki, K. Suzuya, H. Tanaka, Y. Moritomo, T. Matsunaga, N. Yamada, Y. Tanaka, H. Suematsu, M. Takata, *Appl. Phys. Lett.* **2006**, *89*, 201910.
[48] J. Akola, R. O. Jones, *Phys. Rev. B* **2007**, *76*, 235201.
[49] S. Caravati, M. Bernasconi, T. D. Kühne, M. Krack, M. Parrinello, *Appl. Phys. Lett.* **2007**, *91*, 171906.
[50] M. Xu, Y. Cheng, H. Sheng, E. Ma, *Phys. Rev. Lett.* **2009**, *103*, 195502.
[51] J. Hegedüs, S. R. Elliott, *Nat. Mater.* **2008**, *7*, 399.
[52] D. Loke, T. H. Lee, W. J. Wang, L. P. Shi, R. Zhao, Y. C. Yeo, T. C. Chong, S. R. Elliott, *Science* **2012**, *336*, 1566.
[53] T. H. Lee, S. R. Elliott, *Phys. Rev. Lett.* **2011**, *107*, 145702.
[54] J. Kalikka, J. Akola, J. Larrucea, R. O. Jones, *Phys. Rev. B* **2012**, *86*, 144113.
[55] J. Kalikka, J. Akola, R. O. Jones, *Phys. Rev. B* **2016**, *94*, 134105.

**ADVANCED
SCIENCE NEWS**

www.advancedsciencenews.com

pssrrl

physica status solidi

www.pss-rapid.com

[56] J. Akola, R. O. Jones, *Science* **2017**, *358*, 1386.

[57] I. Ronneberger, W. Zhang, H. Eshet, R. Mazzarello, *Adv. Funct. Mater.* **2015**, *25*, 6407.

[58] I. Ronneberger, W. Zhang, R. Mazzarello, *MRS Commun.* **2018**, *8*, 1018.

[59] Y.-R. Guo, F. Dong, C. Qiao, J. J. Wang, S. Y. Wang, M. Xu, Y. X. Zheng, R. J. Zhang, L. Y. Chen, C. Z. Wang, K. M. Ho, *Phys. Chem. Chem. Phys.* **2018**, *20*, 11768.

[60] F. Rao, K. Ding, Y. Zhou, Y. Zheng, M. Xia, S. Lv, Z. Song, S. Feng, I. Ronneberger, R. Mazzarello, W. Zhang, E. Ma, *Science* **2017**, *358*, 1423.

[61] G. M. Zewdie, Y.-X. Zhou, L. Sun, F. Rao, V. L. Deringer, R. Mazzarello, W. Zhang, *Chem. Mater.* **2019**, *31*, 4008.

[62] B. Chen, Y. Chen, K. Ding, K. Li, F. Jiao, L. Wang, I. Zeng, J. Wang, X. Shen, W. Zhang, F. Rao, E. Ma, *Chem. Mater.* **2019**, *31*, 8794.

[63] Y. Zhou, L. Sun, G. M. Zewdie, R. Mazzarello, V. L. Deringer, E. Ma, W. Zhang, *J. Mater. Chem. C* **2020**, *8*, 3646.

[64] S. Hu, B. Liu, Z. Li, J. Zhou, Z. Sun, *Comput. Mater. Sci.* **2019**, *165*, 51.

[65] S. Hu, J. Xiao, J. Zhou, S. R. Elliott, Z. Sun, *J. Mater. Chem. C* **2020**, *8*, 6672.

[66] X.-P. Wang, X.-B. Li, N.-K. Chen, J. Bang, R. Nelson, C. Ertural, R. Dronskowski, H.-B. Sun, S. Zhang, *npj Comput. Mater.* **2020**, *6*, 31.

[67] C. Qiao, Y. R. Guo, S. Y. Wang, M. Xu, X. Miao, C. Z. Wang, K. M. Ho, *Appl. Phys. Lett.* **2019**, *114*, 071901.

[68] B. S. Lee, G. W. Burr, R. M. Shelby, S. Raoux, C. T. Rettner, S. N. Bogle, K. Darmawikarta, S. G. Bishop, J. R. Abelson, *Science* **2009**, *326*, 980.

[69] T. Matsunaga, J. Akola, S. Kohara, T. Honma, K. Kobayashi, E. Ikenaga, R. O. Jones, N. Yamada, M. Takata, R. Kojima, *Nat. Mater.* **2011**, *10*, 129.

[70] M. Salinga, E. Carria, A. Kaldenbach, M. Bornhofft, J. Benke, J. Mayer, M. Wuttig, *Nat. Commun.* **2013**, *4*, 2371.

[71] J. Orava, D. W. Hewak, A. L. Greer, *Adv. Funct. Mater.* **2015**, *25*, 4851.

[72] P. Zalden, C. Bichara, J. van Eijk, C. Braun, W. Bensch, M. Wuttig, *J. Appl. Phys.* **2010**, *107*, 104312.

[73] P. Zalden, F. Quirin, M. Schumacher, J. Siegel, S. Wei, A. Koc, M. Nicoul, M. Trigo, P. Andreasson, H. Enquist, M. Shu, T. Pardini, M. Chollet, D. Zhu, H. Lemke, I. Ronneberger, J. Larsson, A. M. Lindenberg, H. E. Fischer, S. Hau-Riege, D. A. Reis, R. Mazzarello, M. Wuttig, K. Sokolowski-Tinten, *Science* **2019**, *364*, 1062.

[74] F. Rao, W. Zhang, E. Ma, *Science* **2019**, *364*, 1032.

[75] M. S. Arjunan, A. Mondal, A. Das, K. V. Adarsh, A. Manivannan, *Opt. Lett.* **2019**, *44*, 3134.

[76] I. Ronneberger, Y. Chen, W. Zhang, R. Mazzarello, *Phys. Status Solidi RRL* **2019**, *13*, 1800552.

[77] M. Zhu, W. Song, P. M. Konze, T. Li, B. Gault, X. Chen, J. Shen, S. Lv, Z. Song, M. Wuttig, R. Dronskowski, *Nat. Commun.* **2019**, *10*, 3525.

[78] W. Zhang, I. Ronneberger, P. Zalden, M. Xu, M. Salinga, M. Wuttig, R. Mazzarello, *Sci. Rep.* **2014**, *4*, 6529.

[79] W. Zhang, V. L. Deringer, R. Dronskowski, R. Mazzarello, E. Ma, M. Wuttig, *MRS Bull.* **2015**, *40*, 856.

[80] T. Kühne, M. Krack, F. Mohamed, M. Parrinello, *Phys. Rev. Lett.* **2007**, *98*, 066401.

[81] J. Hutter, M. Iannuzzi, F. Schiffmann, J. VandeVondele, *WIREs Comput. Mol. Sci.* **2014**, *4*, 15.

[82] T. D. Kühne, M. Iannuzzi, M. D. Ben, V. V. Rybkin, P. Seewald, F. Stein, T. Laino, R. Z. Khaliullin, O. Schütt, F. Schiffmann, D. Golze, J. Wilhelm, S. Chulkov, M. H. Bani-Hashemian, V. Weber, U. Borštnik, M. Taillefumier, A. S. Jakobovits, A. Lazzaro, H. Pabst, T. Müller, R. Schade, M. Guidon, S. Andermatt, N. Holmberg, G. K. Schenter, A. Hehn, A. Bussy, F. Belleflamme, G. Tabacchi, et al., *J. Chem. Phys.* **2020**, *152*, 194103.

[83] J. P. Perdew, K. Burke, M. Ernzerhof, *Phys. Rev. Lett.* **1996**, *77*, 3865.

[84] S. Goedecker, M. Teter, J. Hutter, *Phys. Rev. B* **1996**, *54*, 1703.

[85] G. Kresse, J. Hafner, *Phys. Rev. B* **1993**, *47*, 558.

[86] G. Kresse, D. Joubert, *Phys. Rev. B* **1999**, *59*, 1758.

[87] T. Hughbanks, R. Hoffmann, *J. Am. Chem. Soc.* **1983**, *105*, 3528.

[88] V. L. Deringer, A. L. Tchougreeff, R. Dronskowski, *J. Phys. Chem. A* **2011**, *115*, 5461.

[89] S. Maintz, V. L. Deringer, A. L. Tchougréeff, R. Dronskowski, *J. Comput. Chem.* **2013**, *34*, 2557.

[90] R. Nelson, C. Ertural, J. George, V. L. Deringer, G. Hautier, R. Dronskowski, *J. Comput. Chem.* **2020**, *41*, 1931.

[91] S. Grimme, J. Antony, S. Ehrlich, H. Krieg, *J. Chem. Phys.* **2010**, *132*, 154104

[92] R. Wang, F. R. L. Lange, S. Cecchi, M. Hanke, M. Wuttig, R. Calarco, *Adv. Funct. Mater.* **2018**, *28*, 1705901.

[93] Y. Zheng, M. Xia, Y. Cheng, F. Rao, K. Ding, W. Liu, Y. Jia, Z. Song, S. Feng, *Nano Res.* **2016**, *9*, 3453.

[94] Y. Xu, X. Wang, W. Zhang, L. Schafer, J. Reindl, F. Vom Bruch, Y. Zhou, V. Evang, J. J. Wang, V. L. Deringer, E. Ma, M. Wuttig, R. Mazzarello, *Adv. Mater.* **2021**, *33*, 2006221.

[95] P. F. Poudeu, M. G. Kanatzidis, *Chem. Commun.* **2005**, *21*, 2672.

[96] S. Cecchi, D. Dragoni, D. Kriegner, E. Tisbi, E. Zallo, F. Arciprete, V. Holý, M. Bernasconi, R. Calarco, *Adv. Funct. Mater.* **2019**, *29*, 1805184.

[97] K. Kifune, Y. Kubota, T. Matsunaga, N. Yamada, *Acta Cryst.* **2005**, *B61*, 492.

[98] S. Ahmed, X. Wang, Y. Zhou, L. Sun, R. Mazzarello, W. Zhang, *arXiv:2101.00789*, **2021**.

[99] S. Caravati, M. Bernasconi, M. Parrinello, *Phys. Rev. B* **2010**, *81*, 014201.

[100] M. Cobelli, M. Galante, S. Gabardi, S. Sanvito, M. Bernasconi, *J. Phys. Chem. C* **2020**, *124*, 9599.

[101] Y. Xie, W. Kim, Y. Kim, S. Kim, J. Gonsalves, M. BrightSky, C. Lam, Y. Zhu, J. J. Cha, *Adv. Mater.* **2018**, *30*, 1705587.

[102] M. Salinga, B. Kersting, I. Ronneberger, V. P. Jonnalagadda, X. T. Vu, M. L. Gallo, I. Giannopoulos, O. Cojocaru-Mirédin, R. Mazzarello, A. Sebastian, *Nat. Mater.* **2018**, *17*, 681.

[103] F. Jiao, B. Chen, K. Ding, K. Li, L. Wang, X. Zeng, F. Rao, *Appl. Mater. Today* **2020**, *20*, 100641.

[104] Z. Cheng, T. Milne, P. Salter, J. S. Kim, S. Humphrey, M. Booth, H. Bhaskaran, *Sci. Adv.* **2021**, *7*, eabd7097.

[105] W. Zhang, E. Ma, *Nat. Mater.* **2018**, *17*, 654.

[106] V. L. Deringer, W. Zhang, M. Lumeij, S. Maintz, M. Wuttig, R. Mazzarello, R. Dronskowski, *Angew. Chem., Int. Ed.* **2014**, *53*, 10817.

[107] Y. Chen, L. Sun, Y. Zhou, G. M. Zewdie, V. L. Deringer, R. Mazzarello, W. Zhang, *J. Mater. Chem. C* **2020**, *8*, 71.

[108] L. Sun, Y. Zhou, X. Wang, Y. Chen, V. L. Deringer, R. Mazzarello, W. Zhang, *npj Comput. Mater.* **2021**, *7*, 29.

[109] T. Siegrist, P. Jost, H. Volker, M. Woda, P. Merkelbach, C. Schlockermann, M. Wuttig, *Nat. Mater.* **2011**, *10*, 202.

[110] W. Zhang, A. Thiess, P. Zalden, R. Zeller, P. H. Dederichs, J. Y. Raty, M. Wuttig, S. Blügel, R. Mazzarello, *Nat. Mater.* **2012**, *11*, 952.

[111] V. Bragaglia, F. Arciprete, W. Zhang, A. M. Mio, E. Zallo, K. Perumal, A. Giussani, S. Cecchi, J. E. Boschker, H. Riechert, S. Privitera, E. Rimini, R. Mazzarello, R. Calarco, *Sci. Rep.* **2016**, *6*, 23843.

[112] M. Wuttig, D. Lusebrink, D. Wamwangi, W. Welnic, M. Gillessen, R. Dronskowski, *Nat. Mater.* **2007**, *6*, 122.

[113] K. Shportko, S. Kremers, M. Woda, D. Lencer, J. Robertson, M. Wuttig, *Nat. Mater.* **2008**, *7*, 653.

[114] M. Zhu, O. Cojocaru-Mirédin, A. M. Mio, J. Keutgen, M. Küpers, Y. Yu, J.-Y. Cho, R. Dronskowski, M. Wuttig, *Adv. Mater.* **2018**, *30*, 1706735.

[115] M. Wuttig, V. L. Deringer, X. Gonze, C. Bichara, J. Y. Raty, *Adv. Mater.* **2018**, *30*, 1803777.

[116] Y. Cheng, O. Cojocaru-Mirédin, J. Keutgen, Y. Yu, M. Küpers, M. Schumacher, P. Golub, J.-Y. Raty, R. Dronskowski, M. Wuttig, *Adv. Mater.* **2019**, *31*, 1904316.

[117] B. J. Kooi, M. Wuttig, *Adv. Mater.* **2020**, *32*, 1908302.

[118] X. Chen, X. Liu, Y. Cheng, Z. Song, *NPG Asia Mater.* **2019**, *11*, 40.

[119] M. Xu, Y. Q. Cheng, L. Wang, H. W. Sheng, Y. Meng, W. G. Yang, X. D. Han, E. Ma, *Proc. Natl. Acad. Sci.* **2012**, *109*, E1055.

[120] W. Zhang, I. Ronneberger, Y. Li, R. Mazzarello, *Chem. Month.* **2014**, *145*, 97.